crystals

MDPI

Article

The Jahn-Teller Distortion at High Pressure: The Case of Copper Difluoride

Dominik Kurzydłowski [1,2]

[1] Centre of New Technologies, University of Warsaw, 02-097 Warsaw, Poland; d.kurzydlowski@cent.uw.edu.pl
[2] Faculty of Mathematics and Natural Sciences, Cardinal Stefan Wyszyński University, 01-038 Warsaw, Poland

Received: 14 February 2018; Accepted: 16 March 2018; Published: 19 March 2018

Abstract: The opposing effects of high pressure (in the GPa range) and the Jahn-Teller distortion led to many intriguing phenomena which are still not well understood. Here we report a combined experimental-theoretical study on the high-pressure behavior of an archetypical Jahn-Teller system, copper difluoride (CuF_2). At ambient conditions this compound adopts a distorted rutile structure of $P2_1/c$ symmetry. Raman scattering measurements performed up to 29 GPa indicate that CuF_2 undergoes a phase transition at 9 GPa. We assign the novel high-pressure phase to a distorted fluorite structure of *Pbca* symmetry, iso-structural with the ambient-pressure structure of AgF_2. Density functional theory calculations indicate that the *Pbca* structure should transform to a non-centrosymmetric $Pca2_1$ polymorph above 30 GPa, which, in turn, should be replaced by a cotunnite phase (*Pnma* symmetry) at 72 GPa. The elongated octahedral coordination of the Cu^{2+} cation persists up to the $Pca2_1$–*Pnma* transition upon which it is replaced by a capped trigonal prism geometry, still bearing signs of a Jahn-Teller distortion. The high-pressure phase transitions of CuF_2 resembles those found for difluorides of transition metals of similar radius (MgF_2, ZnF_2, CoF_2), although with a much wider stability range of the fluorite-type structures, and lower dimensionality of the high-pressure polymorphs. Our calculations indicate no region of stability of a nanotubular polymorph observed for the related AgF_2 system.

Keywords: copper; fluorides; Jahn-Teller effect; high pressure; polymorphism

1. Introduction

In 1937, Jahn and Teller showed that non-linear molecules exhibiting orbital degeneracy will undergo a distortion leading to a lower-energy, and orbitally non-degenerate, structure [1]. The so-called Jahn-Teller (JT) effect is particularly strong in systems containing divalent copper ($3d^9$ electron count). Due to operation of the JT effect the first coordination sphere of the Cu^{2+} cation is distorted and most often forms an elongated instead of a regular octahedron with four shorter equatorial bonds and two longer axial ones [2–4].

The Jahn-Teller effect, also present in compounds containing the iso-electronic Ag^{2+} cation ($4d^9$) [5], has a large impact on material properties such as magnetism [6], and electronic structure [7–9]. Even subtle distortions in the first coordination sphere of the JT-active cation can lead to large changes in material properties, as exemplified by the case of Ag^{2+}-bearing fluorides [10,11]. Due to the fluxional nature of the Jahn-Teller effect many studies have been devoted to tuning this distortion either by chemical substitution [12–16], or by high external pressure [17–22].

In the latter case pressures above 1 GPa (=10 kbar) are used to induce substantial volume reduction which in turn leads to changes in the electronic and structural properties of the studied system. Large compression generally leads to the reduction of the JT distortion; it was found, however, that in compounds containing both Cu^{2+} and Mn^{3+} cations (the latter has a $3d^4$ configuration and is JT-active in the high-spin state) this distortion is surprisingly robust. In $LaMnO_3$ JT-distorted domains persist

up to the insulator-to-metal transition at 34 GPa [18], while for $CsMnF_4$ it was found that the effect is quenched only above 37 GPa when Mn^{3+} cations enter the low-spin state [17]. The JT distortion seems to be even more stable in the case of divalent copper [19,20]. For $CuWO_4$ it initially decreases upon compression, but then increases abruptly during a phase transition at 9.9 GPa, and remains in place up to at least 20 GPa [19]. For Rb_2CuCl_4 it was found that the JT-distorted first coordination sphere of Cu^{2+} is stiffer than the rest of the crystal structure, which leads to tilting distortions at high pressure [20].

In order to elucidate the complex interplay between the effect of large compression and the Jahn-Teller distortions we studied the high pressure phase transitions of copper difluoride (CuF_2). This compound is one of the simplest binary connections containing the Cu^{2+} cation. It belongs to the family of metal difluorides, which have been extensively studied at high pressure [23–37]. Due to the operation of the JT effect CuF_2 adopts at ambient conditions a rarely-encountered crystal structure found only in one other compound (CrF_2) [38].

Here we present experimental and computational evidence that up to 100 GPa CuF_2 undergoes three phase transitions. The four lowest-enthalpy structures can be assigned to the rutile, fluorite, and cotunnite structure families, and the general phase transition sequence found for CuF_2 (rutile $\rightarrow$ fluorite $\rightarrow$ cotunnite) resembles that observed in other difluorides. However due to the operation of the Jahn-Teller effect the coordination of Cu^{2+}, as well as the dimensionality of the structures, differs from that found for other MF_2 systems. The high-pressure phase transitions of CuF_2 are reminiscent of those recently reported for its heavier analogue, AgF_2 [37], with the exception that a nanotubular phase found for AgF_2 is not observed [36].

2. Materials and Methods

Copper difluoride supplied by Sigma-Aldrich (Saint Louis, Missouri, United States) in a form of a powder (98% purity) was used in the study. Due to its hygroscopic nature all loadings were performed in an argon-filled glovebox with both water and oxygen content below 0.5 ppm. Measurements at ambient condition were performed on samples flame-sealed in quartz capillaries (OD 0.3 mm). The purity of the sample was confirmed by powder X-ray diffraction measurements (see Figure S1 in Supplementary Materials).

Raman spectra were acquired with the use of the Alpha300M+ system (Witec Gmbh, Ulm, Germany). We used a 532 nm laser line (35 mW power at sample) delivered to a confocal microscope by a single-mode optical fiber. The signal was collected through a 20$\times$ long working distance objective, and passed through a multi-mode optical fiber to a lens-based spectrometer (Witec UHTS 300, f/4 aperture and a focal length of 300 mm) coupled with an Andor iDUS 401 detector (Oxford Instruments, Abingdon-on-Thames, UK). The spectra were collected with the use of a 1800 mm grating resulting in a 1.5 cm^{-1} spectral resolution.

A total of three high-pressure runs were conducted with the use of a diamond anvil cell (DAC) supplied by D'Anvils (Hod-Hasharon, Israel). The DAC was equipped with low-fluorescence Ia diamonds (single-beveled with culet sizes of 400 µm and 500 µm) and a pre-indented stainless-steel gasket (35 µm thick). The gasket hole of 250 µm was drilled by spark-erosion. The pressure was determined from the shift of the R1 ruby fluorescence line [39]. The position of Raman bands was established with Fityk 0.9.8 software (Marcin Wojdyr, Poland) by background subtraction and fitting of the observed spectra with Lorentzian profiles [40].

Periodic DFT calculations utilized the rotationally-invariant DFT+U method [41], with the PBE exchange-correlation functional [42]. We set the U and J values of the DFT+U method to 7 eV and 0.9 eV, respectively, as suggested in a recent study on $KCuF_3$ [43]. These value are similar to those used in other studies [44,45]. The employed method yielded lattice constants and Cu-F bond lengths overestimated by less than 2% compared to the experimental structure of CuF_2 determined at low temperature [46].

The projector–augmented-wave (PAW) method was used [47], as implemented in the VASP 5.4 code. The cutoff energy of the plane waves was set to 920 eV with a self-consistent-field convergence criterion of 10^{-6} eV. Valence electrons (Zn, Cu: 3d, 4s; F: 2s, 2p) were treated explicitly, while standard VASP pseudopotentials (accounting for scalar relativistic effects) were used for the description of core electrons. The k-point mesh was set at $2\pi \times 0.03$ Å^{-1}. All structures were optimized using a conjugate-gradient algorithm until the forces acting on the atoms were smaller than 5 meV/Å. For each structure the optimization was performed for the lowest-energy spin state, that is: (i) AFM ordering within [$CuF_{4/2}$] sheets for $P2_1/c$, *Pbca*, and $Pca2_1$; (ii) FM ordering within chains of the cotunnite *Pnma* structure; and (iii) AFM ordering within nanotubes present in the *Pbcn* polymorph.

Evolutionary algorithm searches were performed at 20, 60, and 100 GPa for $Z = 8$ with XtalOpt software (version r9 [48]) which was coupled with the DFT+U method described above. The searches yielded the $Pbca/Pca2_1/Pnma$ structures as the lowest-enthalpy polymorphs of CuF_2 at 20/60/100 GPa, in accordance with results presented in this work.

Calculations of Γ-point vibration frequencies were conducted in VASP within the DFT finite-displacement method (0.007 Å displacement was used) and a tighter SCF convergence (10^{-8} eV). Visualization of all structures was performed with the VESTA software package [49]. For symmetry recognition we used the FINDSYM program [50]. Group theory analysis of the vibrational modes was performed with the use of the Bilbao Crystallographic Server [51].

3. Results

3.1. Ambient Pressure

At ambient conditions CuF_2 crystallizes in a structure belonging to the rutile-type family. The rutile (TiO_2) aristotype, adopted by most of the first row transition metal difluorides, has tetragonal ($P4_2/mnm$) symmetry, and features a six-fold coordination of the metal center (Figure 1a). Due to operation of a collective JT distortion copper difluoride adopts a structure with lower symmetry (monoclinic, $P2_1/n$), exhibiting a 4 + 2 coordination of Cu^{2+} [46,52–55]. This structure, shown in Figure 1b, can be also transformed to a $P2_1/c$ setting (Figure 1c) which more clearly illustrates the presence of puckered sheets of [$CuF_{4/2}$] stoichiometry. These sheets host a relatively strong antiferromagnetic (AFM) interaction between the neighboring Cu^{2+} sites [56], which together with a weak ferromagnetic (FM) inter-layer coupling leads to a spin-canted 2D AFM state below 70 K [46,57,58]. Hereinafter when referring to the ambient pressure rutile-type structure of CuF_2 we will use the $P2_1/c$ setting.

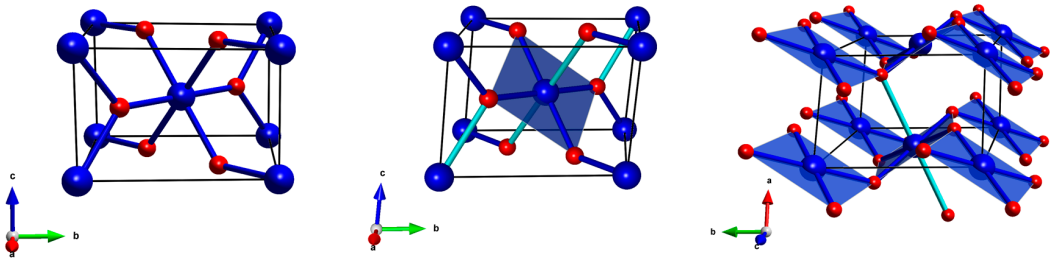

(**a**) (**b**) (**c**)

Figure 1. (**a**) The rutile aristotype ($P4_2/mnm$); (**b**) The CuF_2 structure in the $P2_1/n$ setting; and (**c**) the same structure in the $P2_1/c$ setting. Blue/red balls mark metal/ligand atoms (Cu/F in case of CuF_2); for CuF_2 dark blue cylinders depict short Cu-F bonds (1.9 Å); light blue cylinders depict long bonds (2.3 Å).

Up to date various techniques have been employed in the characterization of CuF_2, but to our knowledge there are no reports concerning the Raman spectrum of this material. Group theory analysis of the $P2_1/c$ structure of copper difluoride ($Z = 2$), performed with the use of the Bilbao

Crystallographic Server [51], indicates that among the 18 Γ-point vibrational modes ($3A_g + 6A_u + 3B_g + 6B_u$) six are Raman-active ($3A_g + 3B_g$).

We performed calculations of the Γ-point frequencies for the $P2_1/c$ structure of CuF_2 with the use of the density functional theory with the inclusion of the on-site Coulomb repulsion (DFT+U method, for calculation details see Materials and Methods). The resulting values are compared in Table 1 with those obtained from ambient-pressure Raman measurements (Figure 2). The lowest-energy A_g mode is not observed experimentally as its predicted frequency of 70 cm^{-1} lies below the detection limit of our Raman setup. Two B_g and two A_g modes with calculated frequencies in the 200–350 cm^{-1} range can be assigned to the four strongest Raman bands found in experiment (Figure 2). The frequency of these four bands is on average only 4.7% higher than those predicted theoretically. Finally, the highest-frequency B_g mode is found experimentally at a Raman shift 8.0% higher than predicted from DFT+U. One additional band at 496 cm^{-1} is observed in the Raman spectrum of powder CuF_2. This transition, marked by a star in Figure 2, can be tentatively assigned as an overtone of the strongest A_g mode at 254 cm^{-1}, or as a combination mode of two B_g vibrations at 221 and 293 cm^{-1}.

Table 1. Comparison of calculated (ω_{th}) and experimental (ω_{exp}) Γ-point Raman frequencies (in cm^{-1}) of the rutile-type $P2_1/c$ structure of CuF_2 at ambient pressure. No scaling was applied to the calculated frequencies.

Symmetry	ω_{th}	ω_{exp}
B_g	524	566
Ag	338	355
B_g	280	293
A_g	245	254
B_g	210	221
A_g	70	n.d.

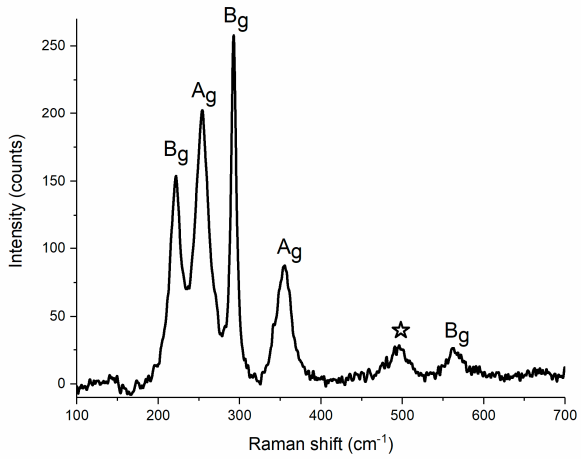

Figure 2. Raman spectrum of powder CuF_2 at ambient condition.

The good accordance between the experimental and theoretical Raman frequencies gives confidence that DFT+U method employed here can accurately simulate the pressure dependence of the frequencies of Raman active modes of CuF_2. In particular the theoretical values should fall close to the experimental ones after scaling by 1.047. This is indeed the case, as will be shown in the subsequent section

3.2. Raman Scattering up to 29 GPa

Powder samples of CuF_2 were loaded into the DAC and compressed to 29.4 GPa with Raman spectra taken upon compression in ca. 2 GPa intervals (for more details see Materials and Methods section). At high pressure all of the observed Raman modes shift to higher frequencies and broaden

(Figure 3a). Around 9 GPa a splitting of the highest-frequency A_g band is observed, as well as a new band appears at 185 cm^{-1} signaling changes in the structure of CuF_2 (Figure 3b, see also Figure S2 in Supplementary Materials, for a deconvolution of the Raman spectra at 19.6 GPa). As we will argue below the changes in the Raman pattern at 9 GPa are a result of a phase transition from the ambient pressure rutile-type $P2_1/c$ structure to a fluorite-like polymorph of *Pbca* symmetry.

Before we discuss this transition we note that the pressure dependence of the Raman frequencies below 9 GPa is in very good agreement with that predicted theoretically for the $P2_1/c$ structure. Interestingly, the lowest-frequency A_g mode (not observed experimentally) is predicted to soften upon compression. This behavior resembles the one found in compounds adopting at ambient conditions the rutile aristotype, for example ZnF_2 [24], CoF_2 [28,31], FeF_2 [30], and MnF_2 [33]. In these systems the pressure-induced softening of a low-frequency B_{1g} mode leads to a second order phase transition from the $P4_2/mnm$ structure to a $CaCl_2$-type polymorph (*Pnnm* symmetry, $Z = 2$). The latter structure can be obtained from the rutile aristotype by introducing tilts of the MF_6 octahedra about the ***c*** axis (compare Figure 1a).

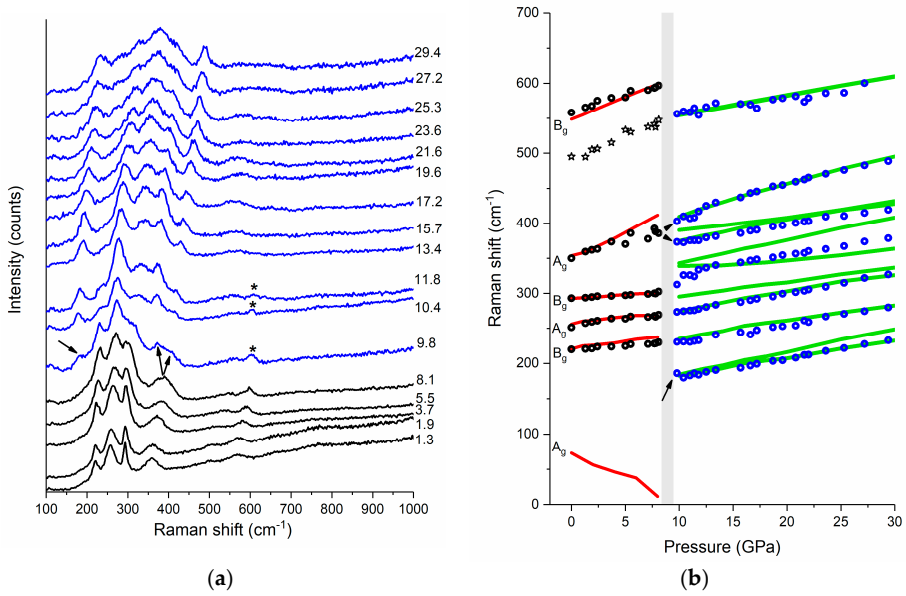

(**a**) (**b**)

Figure 3. (**a**) Raman spectrum of powder CuF_2 at selected pressures (their values are given in GPa), the spectra corresponding to the rutile $P2_1/c$ phase are shown in black while those assigned to the fluorite-type *Pbca* phase are shown in blue; and (**b**) pressure dependence of the frequency of the Raman bands (circles for experiment: black—$P2_1/c$; blue—*Pbca*; lines for DFT+U calculations: red—$P2_1/c$; green—*Pbca*). Arrows mark the appearance of a new low-frequency band and splitting of the A_g band. Asterisks in (**a**) mark the B_g band originating from traces of the $P2_1/c$ structure still present above the phase transition, while stars in (**b**) indicate the pressure dependence of the A_g overtone or B_g combination mode of rutile CuF_2 (see text). The calculated frequencies were scaled by 1.047.

One might, therefore, expect that the ambient-pressure $P2_1/c$ structure of CuF_2 will undergo a similar transition. Indeed in our calculations we find another structure of $P2_1/c$ symmetry and $Z = 2$ which is related to the ambient-pressure structure by rotation of the CuF_6 units about the ***a*** axis (compare Figure 1c). At 9 GPa this polymorph, which we will refer to as $P2_1/c$ (*I*), has a marginally lower enthalpy than $P2_1/c$ ($\Delta H = -1.4$ meV per f.u.). We note, however, that the frequency of its Raman modes is very similar to that of the original $P2_1/c$ structure (differences not exceeding 3%), with the exception of the lowest-frequency A_g mode which is shifted from 11 cm^{-1} for $P2_1/c$ to 74 cm^{-1} for $P2_1/c$ (*I*). Hence the Raman bands predicted for $P2_1/c$ *(I)* cannot account for the changes observed in the spectral region above 100 cm^{-1}.

A possible candidate for the high-pressure polymorph of CuF_2 is a fluorite type structure of *Pbca* symmetry ($Z = 4$, Figure 4a), which is adopted at ambient conditions by AgF_2 [59,60]. Indeed, as can be seen in Figure 3b, in the whole pressure range studied there is a good match between the frequencies of the Raman-active modes predicted for this structure and those observed in experiment. Therefore the phase transition at 9 GPa can be assigned to the transformation from $P2_1/c$ to *Pbca*. This notion is further corroborated by DFT+U calculation which predict a phase transition between these two CuF_2 polymorphs at the same pressure (vide infra). Interestingly the 2D puckered sheets present in $P2_1/c$ are retained in the *Pbca* polymorph (Figure 4a).

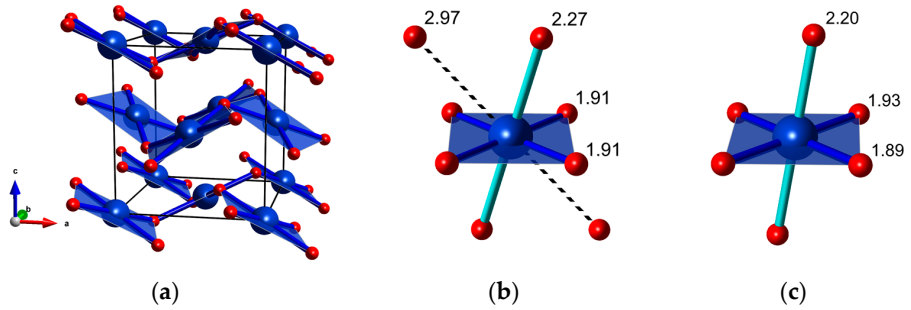

Figure 4. (**a**) The fluorite-type *Pbca* structure CuF_2 (for clarity only the four shortest Cu-F bonds are shown); (**b**) the coordination of Cu^{2+} in *Pbca* calculated at 9 GPa; and (**c**) the coordination of Cu^{2+} in $P2_1/c$ calculated at 9 GPa; Cu-F distances are given in Å.

The *Pbca* structure can be related to the fluorite aristotype (CaF_2, *Fm-3m* symmetry, $Z = 4$) [37]. Therefore the high-pressure transition from rutile-type $P2_1/c$ to *Pbca* is analogous to the rutile-fluorite transition found in difluorides containing non-JT ions (e.g., MgF_2 [23], ZnF_2 [26], CoF_2 [31]). The *Pbca* structure exhibits a 4 + 2 + 2 coordination of Cu^{2+} with two Cu-F contacts considerably longer (≈30%) than the remaining six. Therefore the number of neighbors in the first coordination sphere of Cu^{2+} (6) remains unchanged upon transition from P_1/c to *Pbca*.

3.3. Calculations up to 100 GPa

In order to further validate the interpretation of experiment, and to extend our study to higher pressures we performed DFT+U calculations for various CuF_2 phases up to a pressure of 100 GPa. Apart from the $P2_1/c$ and *Pbca* polymorphs mentioned earlier we took into account three other possible structures: $Pca2_1$ ($Z = 4$, Figure 5a), *Pbcn* ($Z = 8$, Figure 5b), and *Pnma* ($Z = 4$, Figure 5c). These structure were proposed as high-pressure polymorphs of AgF_2 with $Pca2_1$ and *Pbcn* indeed observed experimentally [36,37]. We also searched for other candidate structures with the use of the XtalOpt evolutionary algorithm [48], but did not find any structure competitive in terms of enthalpy with the five mentioned above.

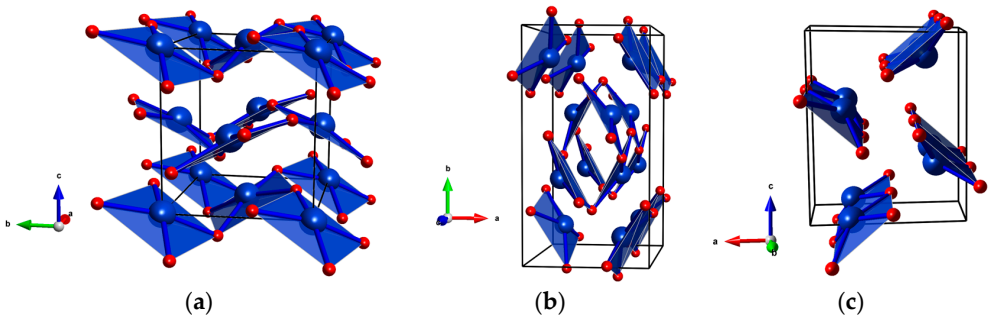

Figure 5. Possible high-pressure structures of CuF_2 (**a**) $Pca2_1$ ($Z = 4$); (**b**) *Pbcn* ($Z = 8$); and (**c**) *Pnma* ($Z = 4$). For clarity only the four shortest Cu-F bonds are shown.

For AgF_2, the $Pca2_1$ polymorph (HP1-AgF_2) is stable between 9 and 14 GPa (Figure 5a). This structure arises from a phonon instability of the ambient-pressure *Pbca* polymorph stable up to 9 GPa [37]. These two fluorite-type structures are closely related and both feature 2D sheets. The main difference between $Pca2_1$ and *Pbca* is that, in the former structure, the metal cations are displaced out of the plane formed by the four nearest F atoms which results in a non-centrosymmetric coordination of the metal cation

The *Pbcn* polymorph (HP2-AgF_2), observed for AgF_2 from 15 GPa up to at least 36 GPa [36,37], features nanotubes built from AgF_4 plaquettes distorted in the same way as in $Pca2_1$ (Figure 5b). Finally, the *Pnma* structure consists of chains built from analogous AgF_4 units (Figure 5c). The *Pnma* phase is isostructural with the cotunnite (α-$PbCl_2$) aristotype, a structure featuring nine-fold coordination of the metal center. The α-$PbCl_2$ polytype is adopted by many metal difluorides at large compression [27]. The *Pbcn* phase also belongs to the cotunnite structure family [37].

Optimization of the $Pca2_1$, *Pbcn*, and *Pnma* structures assuming a CuF_2 stoichiometry does not lead to changes in the bonding topology between fluorine atoms and metal centers with respect to that found in the respective AgF_2 polymorphs. By performing calculations at various pressures we were able to extract and compare the enthalpy of each of the five studied phases up to 100 GPa. In accordance with experiment we find that at ambient conditions (p $\approx$ 0 GPa) the $P2_1/c$ rutile-type structure is the lowest energy polymorph of CuF_2 (Figure 6a). Calculations indicate that at 9 GPa CuF_2 should undergo a phase transition from $P2_1/c$ to *Pbca*, in accordance with the high-pressure experimental results presented in the previous section. We predict a substantial volume decrease (14%) at this transition (Figure 6b).

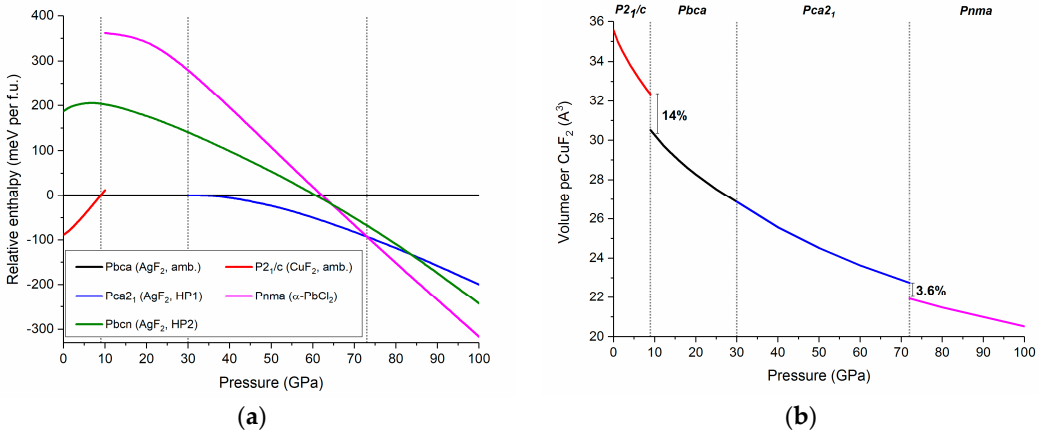

Figure 6. (**a**) The pressure dependence of the relative enthalpies (referenced to that of *Pbca*) of various CuF_2 high-pressure polymorphs; and (**b**) the pressure dependence of the volume per one CuF_2 unit. Dotted lines mark $P2_1/c \rightarrow Pbca$, $Pbca \rightarrow Pca2_1$, and $Pca2_1 \rightarrow Pnma$ phase transition predicted at 9, 30, and 72 GPa, respectively.

Upon further compression *Pbca* is predicted to transform into the $Pca2_1$ polymorph at 30 GPa. The smooth enthalpy change upon the transition, as well as the lack of a volume discontinuity suggests that this is a second order transition, in analogy with what was previously reported for an analogous transition in AgF_2 [37]. The last structural transition, between $Pca2_1$ and *Pnma* is predicted to occur at 72 GPa with a 3.6% volume reduction. We note that in contrast to the $P2_1/c$, *Pbca*, and $Pca2_1$ polymorphs *Pnma* features 1D chains. The calculations indicate no region of stability for the nanotubular *Pbcn* phase which is observed for AgF_2.

For the rutile ($P2_1/c$) and fluorite (*Pbca*) phases of CuF_2 we fitted the calculated volumes with the Birch-Murnaghan equation of state [61]. The obtained values of the bulk modulus (B_0), given in Table 2, indicate that, surprisingly, the low-pressure $P2_1/c$ structure is less compressible than the rutile-like polymorph (at the same time $P2_1/c$ has a larger volume than *Pbca*). The B_0 values calculated

for the CuF_2 phases are about 30% lower than those calculated for the rutile and fluorite phases of ZnF_2 (Table 2). Given the fact that Zn^{2+} has nearly identical radius to Cu^{2+} ($R_{oct}(Zn^{2+})$ = 0.88 Å; $R_{oct}(Cu^{2+})$ = 0.87 Å [62]), one would expect a similar value of B_0 for both CuF_2 and ZnF_2. The lower bulk moduli found for copper difluoride phases most likely stems from the 2D character of its structures which results in facile compression in the direction perpendicular to the sheets. This notion is corroborated by the fact that both $P2_1/c$ and *Pbca* exhibit anisotropic compression with the inter-sheet distances more compressible than the intra-sheet ones (see Figure S3 in the Supplementary Materials).

Table 2. The bulk modulus in GPa (B_0), and its derivative (B_0') calculated for CuF_2 phases. Results obtained for the rutile ($P4_2/mnm$) and fluorite ($Fm\text{-}3m$) structures of ZnF_2 are shown for comparison.

Phase	B_0	B_0'
$P2_1/c$	75	6.1
Pbca	71	5.4
ZnF_2 ($P4_2/mnm$)	101 (105) [1]	4.3
ZnF_2 ($Fm\text{-}3m$)	116 (120) [1]	4.7

[1] DFT calculations with the PBE functional from ref. [32].

We now move to the analysis of the bonding pattern in the high-pressure polymorphs of CuF_2. As can be seen in Figure 7a the Jahn-Teller distortion in $P2_1/c$ is reduced upon compression. This observation is further corroborated by comparing the compressibility of M-F distances in CuF_2 and ZnF_2 (see Figures S4 and S5 in Supplementary Materials). As mentioned earlier the number of neighbors in the first coordination sphere of Cu^{2+} remains at six upon the $P2_1/c$ to *Pbca* transition. This can be well seen in the pressure dependence of Cu-F contacts shown in Figure 7a. It is noteworthy to point out that the distortion of the CuF_6 octahedron becomes larger at the transition. This signals an increase of the JT effect upon the $P2_1/c$–*Pbca* phase transition in analogy to what was found for $CuWO_4$ [19].

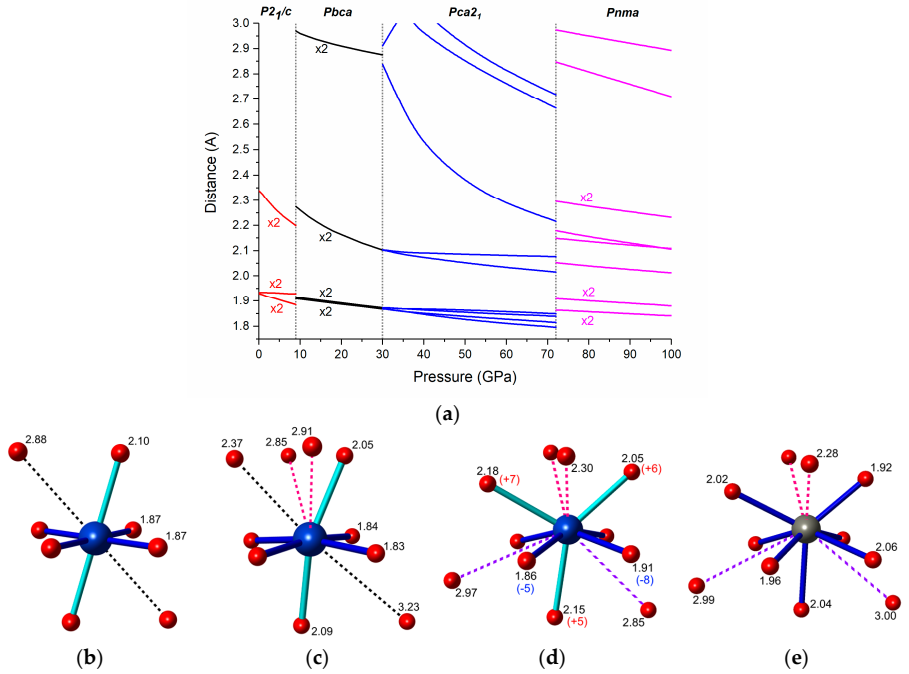

Figure 7. (**a**) Calculated pressure dependence of the Cu-F distances in the high-pressure polymorphs of CuF_2. The coordination of the Cu^{2+} cation in (**b**) *Pbca* at 30 GPa; (**c**) $Pca2_1$ at 50 GPa; and (**d**) *Pnma* at 72 GPa; together with (**e**) the Zn^{2+} coordination in the *Pnma* phase of ZnF_2 optimized at 72 GPa. Distances are given in Å; numbers in parentheses indicate the percentage difference between the Cu-F and Zn-F distances in the *Pnma* polymorphs.

The elongated octahedral coordination is also retained during the *Pbca*-*Pca2*$_1$ transition, although due to additional secondary contacts the CuF_6 units become more distorted in *Pca2*$_1$ (compare Figure 7b,c). Upon compression of *Pca2*$_1$ one of the Cu-F contacts in the second coordination sphere of Cu^{2+} shortens considerably (by 22% from 30 to 72 GPa), and at 72 GPa is only 6.7% longer than the longer of the two Cu-F axial bonds.

The most dramatic changes in the coordination of Cu^{2+} are seen upon the *Pca2*$_1$-*Pnma* transition. The four short equatorial bonds, and the two axial ones elongate upon the transition. Additionally, the longer axial bond becomes nearly equal in length with one of the secondary Cu-F contacts (compare Figure 7c,d). As a result the first coordination sphere of Cu^{2+} can no longer be described as a distorted octahedron, but rather as a capped trigonal prism (coordination number equal to 7). In fact, it closely resembles that of the Zn^{2+} cation in the same *Pnma* phase of ZnF_2 (Figure 7d,e). This might suggest that the Jahn-Teller effect, present in the *P2*$_1$*/c*, *Pbca*, and *Pca2*$_1$ phases, is quenched in the *Pnma* phase.

However, the four shortest Cu-F bonds in *Pnma* (dark blue cylinders in Figure 7d) are 5% to 8% shorter than the corresponding distances in ZnF_2, while the three longer bonds (light blue cylinders) are longer by approximately the same amount. Those differences in the coordination spheres of Cu^{2+} and Zn^{2+} resemble the Jahn-Teller effect found for the octahedral environment. Therefore, it is highly probable that the JT effect is still operational in the *Pnma* phase of CuF_2, although in a different coordination environment. We note that in our calculations that magnetic moments on Cu^{2+} atoms (m_{Cu}), as well as a substantial the band gap (E_g) are retained in the *Pnma* polymorph even at 100 GPa (m_{Cu} = 0.83 μ_B, E_g = 2.4 eV). Moreover the shape of the spin-density of *Pnma* at this pressure (Figure S6 in Supplementary Materials) suggests occupation of a local $d(x^2 - y^2)$ orbital on each Cu^{2+} site, in analogy with the situation found for an elongated octahedral coordination of a d^9 cation.

4. Discussion

The high-pressure transformations of CuF_2 can be compared to that of other metal difluorides, in particular those containing cations of similar size [62]: Mg^{2+} (0.86 Å), Zn^{2+} (0.88 Å), and Co^{2+} (0.89 Å in the high-spin state). The MF_2 systems (M = Mg, Zn, Co), all adopting the undistorted rutile structure at ambient conditions, exhibit a similar phase transition sequence upon compression [23,26,31]: rutile (*P4*$_2$*/mnm*) → $CaCl_2$-type (distorted rutile, *Pnnm*) → HP-PdF_2 (distorted fluorite, *Pa-3*) → α-$PbCl_2$ (cotunnite, *Pnma*). Only in the case of CoF_2 an additional undistorted fluorite phase (*Fm-3m*) exhibits a region of stability between the HP-PdF_2 and α-$PbCl_2$ phases [31].

The corresponding transition pressures are summarized and compared with that of CuF_2 in Figure 8. The subsequent high-pressure transitions of CuF_2 from rutile *P2*$_1$*/c* to fluorite *Pbca* and *Pca2*$_1$ up to cotunnite *Pnma* matches that found for MF_2 (M = Mg, Zn, Co). The differences between copper difluoride and other systems lies in the lower symmetry of CuF_2 phases, which is a result of the JT effect. Moreover, for CuF_2, the stabilization pressure of the cotunnite structure is shifted to much higher pressures compared to the MF_2 systems.

The *Pbca* → *Pca2*$_1$ phase transition predicted to occur at 30 GPa for CuF_2 is analogous to that found at 9 GPa for its heavier analogue, AgF_2 [37]. The difference between the two compounds lies in the fact that for CuF_2 the *Pca2*$_1$ polymorph is predicted to transform to the cotunnite *Pnma* phase at 72 GPa, while for AgF_2 *Pca2*$_1$ transforms to a nanotubular cotunnite-like *Pbcn* structure at 14 GPa. Calculations on the AgF_2 system indicate that *Pnma* and *Pbcn* polymorphs become nearly degenerate in terms of enthalpy above 50 GPa [37]. We do find for CuF_2 that *Pbcn* is more stable than *Pnma* below 64 GPa (see Figure 6a), but at this pressure both are less stable than the *Pca2*$_1$ polymorph, and above this pressure *Pnma* is more stable.

In conclusion, Raman measurements indicate that CuF_2 undergoes a phase transition at 9 GPa between the rutile-type *P2*$_1$*/c* structure and the fluorite-type *Pbca* structure. This result is corroborated by DFT+U calculations, which further indicate that, at 30 GPa, it should transform to a structurally-related *Pca2*$_1$ polymorph. Upon further compression copper difluoride should adopt a cotunnite *Pnma* structure at 72 GPa. Due to the low dimensionality of its high-pressure phases CuF_2

should be more compressible than ZnF_2. Surprisingly for CuF_2 high pressure induces a transition from 2D structure ($P2_1/c$, *Pbca*, $Pca2_1$) t0 a 1D polymorph (*Pnma*).

The classical Jahn-Teller effect leading to an elongated octahedral coordination of Cu^{2+} can be observed in the $P2_1/c$, *Pbca*, and $Pca2_1$ phases up to 72 GPa. Upon entering the *Pnma* phase at that pressure the first coordination sphere of Cu^{2+} changes substantially, but the Jahn-Teller effect seems to be still operational. We hope that our results will motivate further studies into CuF_2 subject to high pressure, in particular measurements which will enable direct probing of the local electronic structure of the Cu^{2+} cations.

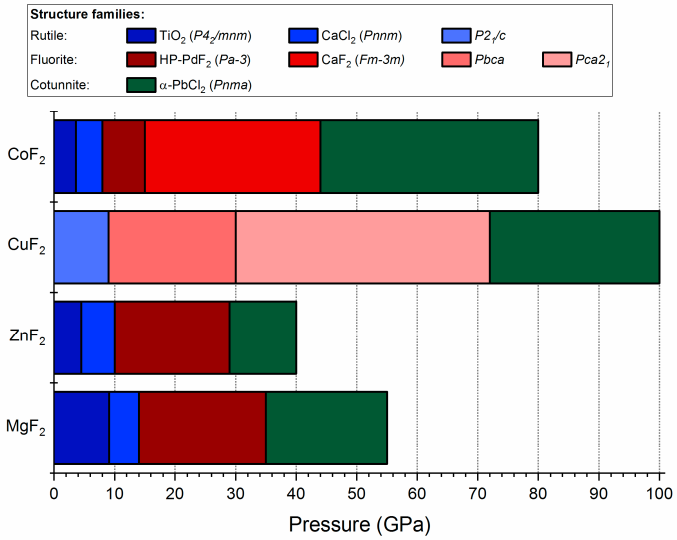

Figure 8. Bar diagram showing the pressure stability intervals of the different structural modifications of MF_2 fluorides. Experimental results for CoF_2, ZnF_2, and MgF_2 are taken from [23,26,31], respectively. The HP-PdF_2 to cotunnite phase transition for ZnF_2 at 29 GPa is taken from our calculations (see Figure S7 in Supplementary Materials).

Supplementary Materials: The following are available online at http://www.mdpi.com/2073-4352/8/3/140/s1, Table S1: Comparison of Γ-point Raman-active modes of ZnF_2 and CuF_2, Figure S1: The experimental powder X-ray diffraction pattern of a sample of CuF_2 together with patterns simulated for the CuF_2 crystal and $CuF_2{\cdot}2H_2O$, Figure S2: The experimental Raman spectrum of CuF_2 together with the deconvolution into Lorentzian profiles, Figure S3: A comparison of the compressibility of inter-sheet and intra-sheet Ag-Ag distances in $P2_1/c$ and *Pbca*, Figure S4: A omparison of the eigenvectors of the B_{2g} mode of ZnF_2, and the symmetry-related B_g mode of CuF_2, Figure S5: Calculated pressure evolution of the difference between the Zn-F/Cu-F bonds together with the predicted differences in the frequencies of the highest B_g mode of CuF_2 and the B_{2g} mode of ZnF_2, Figure S6: A comparison of the spin-density calculated for *Pbca* at 30 GPa and *Pnma* at 100 GPa, Figure S7: The pressure dependence of the relative enthalpy of the cotunnite phase of ZnF_2 referenced to that of the HP-PdF_2 phase.

Acknowledgments: The author acknowledges the support from the Polish National Science Centre (NCN) within grant no. UMO-2014/13/D/ST5/02764. This research was carried out with the support of the Interdisciplinary Centre for Mathematical and Computational Modelling (ICM) University of Warsaw under grant no. GA67-13. Comments from Jakub Gawraczyński and Adam Grzelak are greatly appreciated.

Conflicts of Interest: The author declares no conflict of interest. The founding sponsors had no role in the design of the study; in the collection, analyses, or interpretation of data; in the writing of the manuscript; or in the decision to publish the results.

References

1. Jahn, H.A.; Teller, E. Stability of Polyatomic Molecules in Degenerate Electronic States. I. Orbital Degeneracy. *Proc. R. Soc. A Math. Phys. Eng. Sci.* **1937**, *161*, 220–235. [CrossRef]
2. Reinen, D.; Friebel, C. Local and Cooperative Jahn-Teller Interactions in Model Structures Spectroscopic and Structural Evidence. In *Structural Problems*; Springer: Berlin/Heidelberg, Germany, 1979; Volume 37, pp. 1–60.

3. Falvello, L.R. Jahn–Teller effects in solid-state co-ordination chemistry. *Dalton Trans.* **1997**, 4463–4476. [CrossRef]
4. Halcrow, M.A. Jahn-Teller distortions in transition metal compounds, and their importance in functional molecular and inorganic materials. *Chem. Soc. Rev.* **2013**, *42*, 1784–1795. [CrossRef] [PubMed]
5. Mazej, Z.; Kurzydłowski, D.; Grochala, W. Unique Silver(II) Fluorides: The Emerging Electronic and Magnetic Materials. In *Photonic and Electronic Properties of Fluoride Materials*; Tressaud, A., Poeppelmeier, K., Eds.; Elsevier: Amsterdam, The Netherlands, 2016; pp. 231–260. ISBN 9780128016398.
6. Kugel', K.I.; Khomskii, D.I. The Jahn-Teller effect and magnetism: Transition metal compounds. *Sov. Phys. Uspekhi* **1982**, *25*, 231–256. [CrossRef]
7. Guennou, M.; Bouvier, P.; Toulemonde, P.; Darie, C.; Goujon, C.; Bordet, P.; Hanfland, M.; Kreisel, J. Jahn-Teller, Polarity, and Insulator-to-Metal Transition in $BiMnO_3$ at High Pressure. *Phys. Rev. Lett.* **2014**, *112*, 75501. [CrossRef] [PubMed]
8. Reinen, D. The Modulation of Jahn–Teller Coupling by Elastic and Binding Strain Perturbations—A Novel View on an Old Phenomenon and Examples from Solid-State Chemistry†. *Inorg. Chem.* **2012**, *51*, 4458–4472. [CrossRef] [PubMed]
9. Bersuker, I.B. The Jahn-Teller and pseudo Jahn-Teller effect in materials science. *J. Phys. Conf. Ser.* **2017**, *833*, 12001. [CrossRef]
10. McLain, S.E.; Dolgos, M.R.; Tennant, D.A.; Turner, J.F.C.; Barnes, T.; Proffen, T.; Sales, B.C.; Bewley, R.I. Magnetic behaviour of layered Ag(II) fluorides. *Nat. Mater.* **2006**, *5*, 561–566. [CrossRef] [PubMed]
11. Kurzydłowski, D.; Derzsi, M.; Mazej, Z.; Grochala, W. Crystal, electronic, and magnetic structures of M_2AgF_4 (M = Na–Cs) phases as viewed from the DFT+U method. *Dalton Trans.* **2016**, *45*, 16255–16261. [CrossRef] [PubMed]
12. Alonso, J.A.; Martínez-Lope, M.J.; Casais, M.T.; Fernández-Díaz, M.T. Evolution of the Jahn-Teller distortion of MnO_6 octahedra in $RMnO_3$ perovskites (R = Pr, Nd, Dy, Tb, Ho, Er, Y): A neutron diffraction study. *Inorg. Chem.* **2000**, *39*, 917–923. [CrossRef] [PubMed]
13. Lufaso, M.W.; Woodward, P.M. Jahn-Teller distortions, cation ordering and octahedral tilting in perovskites. *Acta Crystallogr. B.* **2004**, *60*, 10–20. [CrossRef] [PubMed]
14. Goodenough, J.B. Electronic and ionic transport properties and other physical aspects of perovskites. *Rep. Prog. Phys.* **2004**, *67*, 1915–1993. [CrossRef]
15. Kurzydłowski, D.; Mazej, Z.; Grochala, W. Na_2AgF_4: 1D antiferromagnet with unusually short $Ag^{2+}\cdots Ag^{2+}$ separation. *Dalton Trans.* **2013**, *42*, 2167–2173. [CrossRef] [PubMed]
16. Kurzydłowski, D.; Jaroń, T.; Ozarowski, A.; Hill, S.; Jagličić, Z.; Filinchuk, Y.; Mazej, Z.; Grochala, W. Local and Cooperative Jahn–Teller Effect and Resultant Magnetic Properties of M_2AgF_4 (M = Na–Cs) Phases. *Inorg. Chem.* **2016**, *55*, 11479–11489. [CrossRef] [PubMed]
17. Aguado, F.; Rodríguez, F.; Núñez, P. Pressure-induced Jahn-Teller suppression and simultaneous high-spin to low-spin transition in the layered perovskite $CsMnF_4$. *Phys. Rev. B* **2007**, *76*, 94417. [CrossRef]
18. Baldini, M.; Struzhkin, V.V.; Goncharov, A.F.; Postorino, P.; Mao, W.L. Persistence of Jahn-Teller Distortion up to the Insulator to Metal Transition in $LaMnO_3$. *Phys. Rev. Lett.* **2011**, *106*, 66402. [CrossRef] [PubMed]
19. Ruiz-Fuertes, J.; Segura, A.; Rodríguez, F.; Errandonea, D.; Sanz-Ortiz, M.N. Anomalous High-Pressure Jahn-Teller Behavior in $CuWO_4$. *Phys. Rev. Lett.* **2012**, *108*, 166402. [CrossRef] [PubMed]
20. Aguado, F.; Rodríguez, F.; Valiente, R.; Itiè, J.-P.; Hanfland, M. Pressure effects on Jahn-Teller distortion in perovskites: The roles of local and bulk compressibilities. *Phys. Rev. B* **2012**, *85*, 100101. [CrossRef]
21. Calestani, G.; Orlandi, F.; Mezzadri, F.; Righi, L.; Merlini, M.; Gilioli, E. Structural evolution under pressure of $BiMnO_3$. *Inorg. Chem.* **2014**, *53*, 8749–8754. [CrossRef] [PubMed]
22. Friedrich, A.; Winkler, B.; Morgenroth, W.; Perlov, A.; Milman, V. Pressure-induced spin collapse of octahedrally coordinated Mn^{3+} in the tetragonal hydrogarnet henritermierite $Ca_3Mn_2[SiO_4]_2$ $[O_4\ H_4]$. *Phys. Rev. B* **2015**, *92*, 014117. [CrossRef]
23. Haines, J.; Léger, J.M.; Gorelli, F.; Klug, D.D.; Tse, J.S.; Li, Z.Q. X-ray diffraction and theoretical studies of the high-pressure structures and phase transitions in magnesium fluoride. *Phys. Rev. B* **2001**, *64*, 134110. [CrossRef]
24. Perakis, A.; Lampakis, D.; Boulmetis, Y.C.; Raptis, C. High-pressure Raman study of the ferroelastic rutile-to-$CaCl_2$ phase transition in ZnF_2. *Phys. Rev. B* **2005**, *72*, 144108. [CrossRef]

25. Wu, X.; Wu, Z. Theoretical calculations of the high-pressure phases of ZnF_2 and CdF_2. *Eur. Phys. J. B* **2006**, *50*, 521–526. [CrossRef]
26. Kusaba, K.; Kikegawa, T. In situ X-ray observation of phase transitions in under high pressure and high temperature. *Solid State Commun.* **2008**, *145*, 279–282. [CrossRef]
27. Dorfman, S.M.; Jiang, F.; Mao, Z.; Kubo, A.; Meng, Y.; Prakapenka, V.B.; Duffy, T.S. Phase transitions and equations of state of alkaline earth fluorides CaF_2, SrF_2, and BaF_2 to Mbar pressures. *Phys. Rev. B* **2010**, *81*, 174121. [CrossRef]
28. Wang, H.; Liu, X.; Li, Y.; Liu, Y.; Ma, Y. First-principles study of phase transitions in antiferromagnetic XF_2 (X = Fe, Co and Ni). *Solid State Commun.* **2011**, *151*, 1475–1478. [CrossRef]
29. Liu, G.; Wang, H.; Ma, Y.; Ma, Y. Phase transition of cadmium fluoride under high pressure. *Solid State Commun.* **2011**, *151*, 1899–1902. [CrossRef]
30. López-Moreno, S.; Romero, A.H.; Mejía-López, J.; Muñoz, A.; Roshchin, I.V. First-principles study of electronic, vibrational, elastic, and magnetic properties of FeF_2 as a function of pressure. *Phys. Rev. B* **2012**, *85*, 134110. [CrossRef]
31. Barreda-Argüeso, J.A.; López-Moreno, S.; Sanz-Ortiz, M.N.; Aguado, F.; Valiente, R.; González, J.; Rodríguez, F.; Romero, A.H.; Muñoz, A.; Nataf, L.; et al. Pressure-induced phase-transition sequence in CoF_2: An experimental and first-principles study on the crystal, vibrational, and electronic properties. *Phys. Rev. B* **2013**, *88*, 214108. [CrossRef]
32. Torabi, S.; Hammerschmidt, L.; Voloshina, E.; Paulus, B. Ab initio investigation of ground-state properties of group-12 fluorides. *Int. J. Quantum Chem.* **2014**, *114*, 943–951. [CrossRef]
33. López-Moreno, S.; Romero, A.H.; Mejía-López, J.; Muñoz, A. First-principles study of pressure-induced structural phase transitions in MnF_2. *Phys. Chem. Chem. Phys.* **2016**, *18*, 33250–33263. [CrossRef] [PubMed]
34. Stavrou, E.; Yao, Y.; Goncharov, A.F.; Konôpková, Z.; Raptis, C. High-pressure structural study of MnF_2. *Phys. Rev. B* **2016**, *93*, 54101. [CrossRef]
35. Barreda-Argüeso, J.A.; Aguado, F.; González, J.; Valiente, R.; Nataf, L.; Sanz-Ortiz, M.N.; Rodríguez, F. Crystal-Field Theory Validity Through Local (and Bulk) Compressibilities in CoF_2 and $KCoF_3$. *J. Phys. Chem. C* **2016**, *120*, 18788–18793. [CrossRef]
36. Grzelak, A.; Gawraczyński, J.; Jaroń, T.; Kurzydłowski, D.; Mazej, Z.; Leszczyński, P.J.; Prakapenka, V.B.; Derzsi, M.; Struzhkin, V.V.; Grochala, W. Metal fluoride nanotubes featuring square-planar building blocks in a high-pressure polymorph of AgF_2. *Dalton Trans.* **2017**, *46*, 14742–14745. [CrossRef] [PubMed]
37. Grzelak, A.; Gawraczyński, J.; Jaroń, T.; Kurzydłowski, D.; Budzianowski, A.; Mazej, Z.; Leszczyński, P.J.; Prakapenka, V.B.; Derzsi, M.; Struzhkin, V.V.; et al. High-Pressure Behavior of Silver Fluorides up to 40 GPa. *Inorg. Chem.* **2017**, *56*, 14651–14661. [CrossRef] [PubMed]
38. Maitland, R.; Jack, K.H. The Crystal Structure and Interatomic Bonding of Chromous and Chromic Fluorides. *Proc. Chem. Soc.* **1957**, *1957*, 232–233.
39. Dewaele, A.; Torrent, M.; Loubeyre, P.; Mezouar, M. Compression curves of transition metals in the Mbar range: Experiments and projector augmented-wave calculations. *Phys. Rev. B* **2008**, *78*, 104102. [CrossRef]
40. Wojdyr, M. Fityk: A general-purpose peak fitting program. *J. Appl. Crystallogr.* **2010**, *43*, 1126–1128. [CrossRef]
41. Liechtenstein, A.I.; Zaanen, J. Density-functional theory and strong interactions: Orbital ordering in Mott-Hubbard insulators. *Phys. Rev. B* **1995**, *52*, R5467. [CrossRef]
42. Perdew, J.P.; Burke, K.; Ernzerhof, M. Generalized Gradient Approximation Made Simple. *Phys. Rev. Lett.* **1996**, *77*, 3865–3868. [CrossRef] [PubMed]
43. Legut, D.; Wdowik, U.D. Vibrational properties and the stability of the $KCuF_3$ phases. *J. Phys. Condens. Matter* **2013**, *25*, 115404. [CrossRef] [PubMed]
44. Pavarini, E.; Koch, E.; Lichtenstein, A.I. Mechanism for Orbital Ordering in $KCuF_3$. *Phys. Rev. Lett.* **2008**, *101*, 266405. [CrossRef] [PubMed]
45. Binggeli, N.; Altarelli, M. Orbital ordering, Jahn-Teller distortion, and resonant x-ray scattering in $KCuF_3$. *Phys. Rev. B* **2004**, *70*, 85117. [CrossRef]
46. Fischer, P.; Hälg, W.; Schwarzenbach, D.; Gamsjäger, H. Magnetic and crystal structure of copper(II) fluoride. *J. Phys. Chem. Solids* **1974**, *35*, 1683–1689. [CrossRef]
47. Blöchl, P.E. Projector augmented-wave method. *Phys. Rev. B* **1994**, *50*, 17953–17979. [CrossRef]

48. Falls, Z.; Lonie, D.C.; Avery, P.; Shamp, A.; Zurek, E. XtalOpt version r9: An open-source evolutionary algorithm for crystal structure prediction. *Comput. Phys. Commun.* **2016**, *199*, 178–179. [CrossRef]
49. Momma, K.; Izumi, F. VESTA: A three-dimensional visualization system for electronic and structural analysis. *J. Appl. Crystallogr.* **2008**, *41*, 653–658. [CrossRef]
50. Stokes, H.T.; Hatch, D.M. FINDSYM: Program for identifying the space-group symmetry of a crystal. *J. Appl. Crystallogr.* **2005**, *38*, 237–238. [CrossRef]
51. Kroumova, E.; Aroyo, M.I.; Perez-Mato, J.M.; Kirov, A.; Capillas, C.; Ivantchev, S.; Wondratschek, H. Bilbao Crystallographic Server: Useful Databases and Tools for Phase-Transition Studies. *Phase Transit.* **2003**, *76*, 155–170. [CrossRef]
52. Billy, C.; Haendler, H.M. The Crystal Structure of Copper(II) Fluoride. *J. Am. Chem. Soc.* **1957**, *79*, 1049–1051. [CrossRef]
53. Taylor, J.C.; Wilson, P.W. The structures of fluorides VI. Precise structural parameters in copper difluoride by neutron diffraction. *J. Less Common Met.* **1974**, *34*, 257–259. [CrossRef]
54. Chatterji, T.; Hansen, T.C. Magnetoelastic effects in Jahn–Teller distorted CrF_2 and CuF_2 studied by neutron powder diffraction. *J. Phys. Condens. Matter* **2011**, *23*, 276007. [CrossRef] [PubMed]
55. Burns, P.C.; Hawthorne, F.C. Rietveld Refinement of the Crystal Structure of CuF_2. *Powder Diffr.* **2013**, *6*, 156–158. [CrossRef]
56. Reinhardt, P.; Moreira, I.D.P.R.; de Graaf, C.; Dovesi, R.; Illas, F. Detailed ab-initio analysis of the magnetic coupling in CuF_2. *Chem. Phys. Lett.* **2000**, *319*, 625–630. [CrossRef]
57. Joenk, R.J.; Bozorth, R.M. Magnetic Properties of CuF_2. *J. Appl. Phys.* **1965**, *36*, 1167–1168. [CrossRef]
58. Boo, W.O.J.; Stout, J.W. Heat capacity and entropy of CuF_2 and CrF_2 from 10 to 300 °K. Anomalies associated with magnetic ordering and evaluation of magnetic contributions to the heat capacity. *J. Chem. Phys.* **1979**, *71*, 9–16. [CrossRef]
59. Fischer, P.; Roult, G.; Schwarzenbach, D. Crystal and magnetic structure of silver difluoride-II. Weak 4d-ferromagnetism of AgF2. *J. Phys. Chem. Solids* **1971**, *32*, 1641–1647. [CrossRef]
60. Jesih, A.; Lutar, K.; Žemva, B.; Bachmann, B.; Becker, S.; Müller, B.G.; Hoppe, R. Einkristalluntersuchungen an AgF2. *Z. Anorg. Allg. Chem.* **1990**, *588*, 77–83. [CrossRef]
61. Birch, F. Finite Elastic Strain of Cubic Crystals. *Phys. Rev.* **1947**, *71*, 809–824. [CrossRef]
62. Shannon, R.D. Revised effective ionic radii and systematic studies of interatomic distances in halides and chalcogenides. *Acta Crystallogr. Sect. A* **1976**, *32*, 751–767. [CrossRef]